






Acousto-optic modulation of a wavelength-scale waveguide: supplement

CHRISTOPHER J. SARABALIS,^{1,2}  RAPHAËL VAN LAER,¹  RISHI N. PATEL,¹  YANNI D. DAHMANI,¹ WENTAO JIANG,¹ FELIX M. MAYOR,¹ AND AMIR H. SAFAVI-NAEINI^{1,3}

¹*Department of Applied Physics and Ginzton Laboratory, Stanford University 348 Via Pueblo Mall, Stanford, California 94305, USA*

²*e-mail: sicamor@stanford.edu*

³*e-mail: safavi@stanford.edu*

This supplement published with The Optical Society on 6 April 2021 by The Authors under the terms of the [Creative Commons Attribution 4.0 License](https://creativecommons.org/licenses/by/4.0/) in the format provided by the authors and unedited. Further distribution of this work must maintain attribution to the author(s) and the published article's title, journal citation, and DOI.

Supplement DOI: <https://doi.org/10.6084/m9.figshare.13952720>

Parent Article DOI: <https://doi.org/10.1364/OPTICA.413401>

Acousto-optic modulation of a wavelength-scale waveguide: supplementary material

CHRISTOPHER J. SARABALIS,^{1,2} RAPHAËL VAN LAER,¹ RISHI N. PATEL,¹ YANNI D. DAHMANI,¹ WENTAO JIANG,¹ FELIX M. MAYOR,¹ AND AMIR H. SAFAVI-NAEINI^{1,3}

Department of Applied Physics and Ginzton Laboratory, Stanford University

348 Via Pueblo Mall, Stanford, California 94305, USA

²*sicamor@stanford.edu*, ³*safavi@stanford.edu*

Abstract: This document provides supplementary information to “Acousto-optic modulation of a wavelength-scale waveguide.” It contains a derivation of the coupled mode equations, interaction rates, and mode orthogonality relations; a generalized analysis of the dynamics including the loss and dephasing with measurements of the optical and RF bandwidth; details on how the acousto-optic multiplexer is characterized; a discussion on the RF power-handling of the piezoelectric transducer; and details on the inference of the interaction rate, g .

© 2021 Optical Society of America

1. Optomechanics in a waveguide

For the ease of the reader, in this appendix we derive the coupled mode theory in Eq. (1) in the manuscript including the form for the coupling coefficient Eq. (3) from Maxwell’s equations. The coupled mode equations used here are essentially the same as those derived by Yariv in 1973 [1] and are a special case of the equations of motion used in the Brillouin scattering literature. In the Brillouin literature, the dynamics of the mechanical field b is on equal-footing with the optical fields a_i . Here, as is appropriate for an acousto-optic modulator, we assume a strong mechanical drive such that b is approximately unaffected by the optical fields. b appears as a non-dynamical parameter in the equations of motion for a_i .

For Brillouin scattering, Sipe and Steel provide a derivation of the coupled mode theory starting with the Hamiltonians for elasticity, electromagnetism, and their parametric optomechanical coupling [2]. This approach allows them to derive a fully quantum theory. Wolff *et al.* derive the classical coupled mode theory from the second-order differential equations of motion for the electric field and mechanical displacement field [3]. Our approach is similar to a special case of that of Wolff *et al.* but is built off the first-order differential form of Maxwell’s equations.

1.1. Coupled-mode theory from Maxwell’s Equations

Maxwell’s equations which generate the motion of the field

$$\nabla \times \mathbf{E} = -\partial_t \mu \mathbf{H} \quad (1)$$

$$\nabla \times \mathbf{H} = \partial_t \epsilon \mathbf{E} \quad (2)$$

can be expressed compactly

$$\nabla \times i\sigma_y \Psi = \partial_t \Pi \Psi \quad (3)$$

by defining the two-component field vector

$$\Psi = \begin{pmatrix} \mathbf{E} \\ \mathbf{H} \end{pmatrix} \quad (4)$$

and the matrix

$$\Pi = \begin{pmatrix} \varepsilon & 0 \\ 0 & \mu \end{pmatrix}. \quad (5)$$

A waveguide with continuous translation symmetry along z has solutions of the form

$$\Psi(t, x, y, z) = \psi(x, y) e^{i\beta z - i\omega t}. \quad (6)$$

For a given ω , the mode profile $\psi(x, y)$ and wavevector β solve the eigenvalue problem

$$(\nabla_{\perp} \times i\sigma_y + i\beta \hat{z} \times i\sigma_y + i\omega \Pi) \psi = 0 \quad (7)$$

following from Eq. (3).

The modes of a waveguide are orthogonal under two inner products as shown in Sections 1.3 and 1.4. Consider two solutions with profiles ψ_i and ψ_j and wavevectors $\beta_i \neq \beta_j$. If Π is Hermitian, *i.e.*, $\Pi = \Pi^\dagger$, the profiles are power-orthogonal

$$-2\mathcal{P}_{ij} = \int dA \psi_i^* \cdot \hat{\mathbf{z}} \times i\sigma_y \psi_j \quad (8)$$

$$= 0 \quad (9)$$

where $\hat{\mathbf{z}} = (\hat{z}, \hat{z})^\top$. In terms of the fields,

$$\mathcal{P}_{ij} = \frac{1}{2} \hat{z} \cdot \int dA \mathbf{e}_i^* \times \mathbf{h}_j + \mathbf{e}_j \times \mathbf{h}_i^* \quad (10)$$

where $\mathbf{e}(x, y)$ and $\mathbf{h}(x, y)$ are the electric and magnetic field profiles, respectively. When $i = j$, this is the z -component of the time-averaged power. Similarly if $\Pi = \Pi^*$ and $[\sigma_z, \Pi] = 0$, the profiles are also energy-orthogonal

$$2\mathcal{E}_{ij} = \int dA \psi_i^* \cdot \Pi \psi_j \quad (11)$$

$$= 0 \quad (12)$$

where

$$\mathcal{E}_{ij} = \frac{1}{2} \int dA \mathbf{e}_i^* \varepsilon \mathbf{e}_j + \mathbf{h}_i^* \mu \mathbf{h}_j \quad (13)$$

is the energy density along z when $i = j$.

The modes of the waveguide give us a basis in which we can express an arbitrary harmonic solution. Now we show, following from our orthogonality relations, that this basis diagonalizes the dynamics yielding a system of independent telegrapher equations. We are primarily interested in the dynamics of waves in a narrowband about ω . In this case, we can decompose the field in our basis of waveguide modes

$$\Psi(t, x, y, z) = \sum_i a_i(t, z) \psi_i(x, y) e^{i\beta_i z - i\omega t} \quad (14)$$

and find the dynamics of the coefficients, or “envelopes,” $a_i(t, z)$. The constraint on the bandwidth of $a_i(t, z)$ is the “slowly varying envelope approximation.” Sipe and Steel describe how higher order corrections to the field can be included in the dynamics [2]. Eq. (14) has a sum over discrete bands but can be generalized to include an integral over a continuum of states, like the radiative modes in the air surrounding our LN waveguide.

Each of the modes $\psi_i \exp(i\beta_i z - i\omega t)$ solves Maxwell's equations and so, if we expand Eq. (3) in this basis, only the derivatives acting on the coefficients $a_i(t, z)$ remain. Acting on each side with $\int dA \psi_i^*$, we use our orthogonality relations to find the equation of motion for a_i

$$(-2\mathcal{P}_{ii}\partial_z - 2\mathcal{E}_{ii}\partial_t) a_i(t, z) = 0. \quad (15)$$

Defining the group velocity $v_i \equiv \mathcal{P}_{ii}/\mathcal{E}_{ii}$, we can re-express this as

$$(v_i^{-1}\partial_t + \partial_z) a_i(t, z) = 0. \quad (16)$$

Finally defining a vector \mathbf{a} with components a_i and matrix \mathbf{v} with diagonal component v_i , we have

$$(\mathbf{v}^{-1}\partial_t + \partial_z) \mathbf{a}(t, z) = 0. \quad (17)$$

In these equations, light in each mode propagates at the mode's group velocity. In the next section, we incorporate physics which modulates and couples the modes.

1.2. Perturbative coupling and inter-modal scattering in optomechanics

Many of the effects in parametrically driven systems and nonlinear optics can be captured in the coupled mode theory by including a polarization drive field to the RHS of the equations [1]. Optomechanics, electro-optics, and thermo-optics are all examples of parametric modulation in which the drive field comes from perturbing the material $\Pi \rightarrow \Pi + \delta\Pi$ such that

$$(v_i^{-1}\partial_t + \partial_z) a_i(t, z) = -\frac{\int dA (\psi_i e^{i\omega t - i\beta_i z})^* \cdot \partial_t \delta\Pi \psi_i}{2\mathcal{P}_{ii}}. \quad (18)$$

For optomechanics, a mechanical field \mathbf{u} perturbs ε such that

$$\varepsilon \rightarrow \varepsilon + \delta_{\mathbf{u}}\varepsilon \cdot \mathbf{u}. \quad (19)$$

The perturbation has a radiation pressure term that is delta-distributed on boundaries between dielectrics ∂R [4] and a photoelastic term [5]

$$\delta_{\mathbf{u}}\varepsilon \cdot \mathbf{u} = (\Delta\varepsilon\mathbf{\Pi}_{\parallel} - \varepsilon\Delta\varepsilon^{-1}\varepsilon\mathbf{\Pi}_{\perp}) (\mathbf{u} \cdot \hat{n}) \delta_{\partial R} \quad (20)$$

$$- \varepsilon \cdot \frac{p\mathbf{S}}{\varepsilon_0} \cdot \varepsilon. \quad (21)$$

Here \hat{n} is normal to the boundary ∂R pointing from dielectric 1 into dielectric 2; $\Delta\varepsilon$ and $\Delta\varepsilon^{-1}$ are $\varepsilon_2 - \varepsilon_1$ and $\varepsilon_2^{-1} - \varepsilon_1^{-1}$; $\mathbf{\Pi}_{\perp}$ and $\mathbf{\Pi}_{\parallel}$ project the field perpendicular and parallel to \hat{n} , respectively; p is the photoelastic tensor; and $S_{ij} = (\partial_i u_j + \partial_j u_i)/2$ is the strain in the deformed medium.

With our expression for the perturbation $\delta\Pi$ for optomechanics, we turn our attention to the case treated in the manuscript: coupling between the TE_0 mode with amplitude a_0 and the TE_1 with amplitude a_1 .

Only phase-matched interactions contribute constructively over long interaction times and distances. Consider the mechanical wave

$$\mathbf{u}(t, x, y, z) = \sqrt{\Phi_m^{-1}} \left(b\mathbf{u}(x, y) e^{iKz - i\Omega t} + \text{c.c.} \right) \quad (22)$$

propagating along $+z$. The amplitude b is taken to be real and constant. The mode is flux normalized where $\Phi_m = \mathcal{P}_m/\hbar\Omega$ such that $|b|^2$ is the phonon flux with units of Hz. If the

mechanical mode phase-matches the TE₀ and TE₁ modes, *i.e.*, $\omega_0 = \omega_1 + \Omega$ and $\beta_0 = \beta_1 + K$, Eq. (18) for the TE₀ amplitude becomes

$$\left(v_1^{-1}\partial_t + \partial_z\right)a_0(t, z) = -ig_{01}ba_1 \quad (23)$$

with

$$g_{01} = -\frac{\omega_0}{2} \frac{\int dA \mathbf{e}_0^* \cdot \delta \mathbf{u} \varepsilon \cdot \mathbf{u} \cdot \mathbf{e}_1}{\mathcal{P}_{00} \sqrt{\Phi_m}}. \quad (24)$$

The RHS describes the action of the co-propagating anti-Stokes process. Similarly, the co-propagating Stokes process drives the a_1 mode

$$\left(v_1^{-1}\partial_t + \partial_z\right)a_1(t, z) = -ig_{10}b^*a_0 \quad (25)$$

with

$$g_{10} = -\frac{\omega_1}{2} \frac{\int dA \mathbf{e}_1^* \cdot \delta \mathbf{u} \varepsilon \cdot \mathbf{u}^* \cdot \mathbf{e}_0}{\mathcal{P}_{11} \sqrt{\Phi_m}}. \quad (26)$$

If we flux normalize the optical modes $\mathcal{P}_i = \hbar\omega_i$ and choose the phase of the mode profiles such that $g \equiv g_{01} = g_{10}$, we arrive at

$$\left(\mathbf{v}^{-1}\partial_t + \partial_z\right)\mathbf{a} = -igb\sigma_x\mathbf{a} \quad (27)$$

for $b = b^*$. This is Eq. (1) in the manuscript. By normalizing by flux, the operator on the RHS of Eq. (27) is anti-Hermitian and therefore the dynamics generated by it are unitary. That means photons are scattered between the two modes, conserving the total photon number. This is the Manley-Rowe relations for the processes considered.

The same formulation is readily adapted to describe other traveling-wave interactions such as electro-optic modulation and non-linear interactions by making a different choice for $\delta\Pi$ or perturbation to the energy $\psi \cdot \delta\Pi\psi/2$ [1].

1.3. Power orthogonality

In order to arrive at the diagonalized telegrapher Eq. (17), we made use of the fact that the mode profiles ψ_i are power- and energy-orthogonal. Solutions to Eq. (7) simultaneously diagonalize the operators $\hat{z} \times i\sigma_y$ and Π . Here we show how these orthogonality relations are derived. Similar derivations can be found for optical waveguides in Snyder and Love [6] and piezoelectric waveguides in Auld [7].

The power- and energy-orthogonality relations are closely related to local conservation of energy. First we derive local conservation of energy from Eq. (3) before deriving from it the orthogonality relations. The operators in Eq. (3) are symmetric under exchange. For any unit vector $\hat{\mathbf{n}} = (\hat{n}, \hat{n})^\top$, the product $\hat{\mathbf{n}} \cdot \Psi_i \times i\sigma_y \Psi_j$ is invariant under $i \leftrightarrow j$

$$\hat{\mathbf{n}} \cdot \Psi_i \times i\sigma_y \Psi_j = \hat{\mathbf{n}} \cdot \Psi_j \times i\sigma_y \Psi_i \quad (28)$$

$$= \hat{n} \cdot \mathbf{E}_i \times \mathbf{H}_j + \hat{n} \cdot \mathbf{E}_j \times \mathbf{H}_i \quad (29)$$

which is manifest when expressed in terms of the fields. Consequently, the divergence takes the symmetric form

$$-\nabla \cdot (\Psi_i \times i\sigma_y \Psi_j) = \Psi_i \cdot \nabla \times i\sigma_y \Psi_j + \Psi_j \cdot \nabla \times i\sigma_y \Psi_i. \quad (30)$$

Substituting in Maxwell's equations we find

$$-\nabla \cdot (\Psi_i \times i\sigma_y \Psi_j) = \partial_t (\Psi_i \Pi \Psi_j). \quad (31)$$

so long as $\Pi = \Pi^\top$ and $\partial_t \Pi = 0$. When $i = j$, this is the source-free form of local conservation of energy (multiplied by 2). A similar result follows when $\Pi = \Pi^\dagger$,

$$-\nabla \cdot (\Psi_i^* \times i\sigma_y \Psi_j) = \partial_t (\Psi_i^* \Pi \Psi_j). \quad (32)$$

Power-orthogonality follows from Eq. (32). Consider two modes Ψ_i and Ψ_j of a waveguide of the form in Eq. (6) with $\omega_i = \omega_j$. In this case, the total time derivative in Eq. (32) vanishes leaving

$$\nabla \cdot (\Psi_i^* \times i\sigma_y \Psi_j) = 0. \quad (33)$$

Since the modes of the waveguide are confined such that $\psi_i^* \times i\sigma_y \psi_j$ vanishes at the boundary of the xy -plane, it follows that

$$(\beta_j - \beta_i) \hat{z} \cdot \int dA \psi_i^* \times i\sigma_y \psi_j = 0. \quad (34)$$

Non-degenerate modes $\beta_i \neq \beta_j$ are power-orthogonal; in a flux-normalized basis, $\mathcal{P}_{ij} = \delta_{ij} \hbar \omega$.

In a similar way we can show that when two modes have equal wavevectors $\beta_i = \beta_j$,

$$(\omega_j - \omega_i) \int dA \psi_i^* \Pi \psi_j = 0. \quad (35)$$

If $\beta_i = \beta_j$ and $\omega_i \neq \omega_j$, the modes are energy-orthogonal. But what we need to show is that the modes are energy-orthogonal when $\omega_i = \omega_j$ and $\beta_i \neq \beta_j$. To do that we need another constraint on the dynamics.

1.4. Energy orthogonality

We employ time-reversal symmetry to show that two modes, i and j , of the same frequency are also energy-orthogonal

$$\int dA \psi_i^* \Pi \psi_j = 0. \quad (36)$$

Consider an electromagnetic field of the form

$$\Psi(t, x, y, z) = \int d\omega \tilde{\Psi}(\omega, x, y, z) e^{-i\omega t}. \quad (37)$$

Under time-reversal \mathbf{T} , each Fourier component of the field state vector becomes

$$\mathbf{T} \tilde{\Psi} = \sigma_z \tilde{\Psi}^*. \quad (38)$$

It follows that \mathbf{T} — specifically σ_z — flips the sign of the “power” operator (LHS of Eq. (3))

$$\sigma_z (\nabla \times i\sigma_y) \sigma_z = -\nabla \times i\sigma_y. \quad (39)$$

In contrast, so long as $[\sigma_z, \Pi] = 0$, the “energy” operator (RHS) does not change sign

$$\sigma_z \partial_t \Pi \sigma_z = \partial_t \Pi. \quad (40)$$

This is what we intuitively expect: reversing time inverts the power without affecting the energy density.

When deriving power-orthogonality, the time-dependence of Ψ_1^* and Ψ_2 cancels such that the total time derivative $\partial_t (\Psi_1^* \Pi \Psi_2)$ vanishes. We use the relative sign flip of the two operators under \mathbf{T} to preserve these energy terms.

If $[\Pi, \sigma_z] = 0$ and $\Pi = \Pi^*$, then the equations are symmetric under time-reversal. Every harmonic solution Ψ (dropping the tildes) maps to a corresponding time-reversed solution $\mathbf{T}\Psi = \sigma_z \Psi^*$. It follows that

$$(\mathbf{T}\Psi_2)^* \cdot (\nabla \times i\sigma_y + \partial_t \Pi) (\mathbf{T}\Psi_1) = 0 \quad (41)$$

and therefore

$$\Psi_2 \cdot (-\nabla \times i\sigma_y + \partial_t \Pi) \Psi_1^* = 0. \quad (42)$$

Subtracting this from

$$\Psi_1^* \cdot (\nabla \times i\sigma_y + \partial_t \Pi) \Psi_2 = 0, \quad (43)$$

we find

$$\nabla \cdot (\Psi_1^* \times i\sigma_y \Psi_2) + \Psi_1^* \partial_t \Pi \Psi_2 - \Psi_2 \partial_t \Pi \Psi_1^* = 0 \quad (44)$$

where instead of the total time derivative in Eq. (31), we have a difference. For waveguide modes, solutions of the form $\psi_i e^{i\beta_i z - i\omega_i t}$, this becomes

$$i(\beta_2 - \beta_1) \hat{z} \cdot \int dA \psi_1^* \times i\sigma_y \psi_2 - i(\omega_1 + \omega_2) \int dA \psi_1^* \Pi \psi_2 = 0 \quad (45)$$

after integrating over the cross-section. When $\omega_1 = \omega_2$ and $\beta_1 \neq \beta_2$, the modes are power-orthogonal and the first term vanishes, leaving us with the energy-orthogonality relation in Eq. (36).

Thus at a fixed-frequency when $\Pi = \Pi^\dagger$, $\Pi = \Pi^*$, and $[\sigma_z, \Pi] = 0$, the modes of a waveguide simultaneously diagonalize the operators in Eq. (3) giving us the independent telegrapher Eqs. (17) and, ultimately, the optomechanically coupled dynamics in Eq. (27).

2. Dynamics with loss and dephasing

The dynamics presented in the text (Eq. (1)) assume the mechanical amplitude b is constant along the waveguide, and the scattering processes are perfectly phase-matched. Here we generalize the model to include loss and dephasing.

2.1. Mechanical loss

If we include mechanical loss in our model, the mechanical amplitude b decays exponentially

$$b(z) = b e^{-\gamma z/2}. \quad (46)$$

In the presence of loss, the steady-state solutions become

$$\mathbf{a}_\pm(z) = \mathbf{a}_\pm(0) \exp \left[\pm i g b \left(\frac{1 - e^{-\gamma b z/2}}{\gamma/2} \right) \right]. \quad (47)$$

This yields the same solutions as before (Eq. (2)) except

$$z \rightarrow \frac{2}{\gamma} \left(1 - e^{-\gamma z/2} \right). \quad (48)$$

We use this to define the effective interaction length

$$L_{\text{eff}} = \frac{2}{\gamma} \left(1 - e^{-\gamma L/2} \right) \quad (49)$$

which asymptotes to $2/\gamma$.

For the SH_0 mode at 440 MHz we measure $\gamma = 11.7$ dB/mm. With this γ , L_{eff} asymptotes to $742 \mu\text{m}$. In the long-device limit, full conversion $\text{TE}_1 \leftrightarrow \text{TE}_0$ requires

$$P_{\pi/2} = \frac{\pi^2}{4t_{\text{b}\mu}^2 g^2 L_{\text{eff}}^2} \quad (50)$$

$$= \frac{36.5 \mu\text{W}}{t_{\text{b}\mu}^2} \quad (51)$$

which, given $t_{\text{b}\mu}^2 = -21.9$ dB, is

$$P_{\pi/2} = 5.65 \text{ mW} \quad (52)$$

incident microwave power. This is roughly three orders of magnitude smaller than a bulk AOM but is $10\times$ larger than the efficiency reported by Hinkov *et al.* [8]. Improvements to g , γ , and $t_{\text{b}\mu}$ are needed to go beyond previous demonstrations. A 10 dB improvement to $|t_{\text{b}\mu}|^2$ is suggested by the -12 dB insertion loss of SH_0 waveguide transducers at 2 GHz [9].

2.2. Dephasing and optical bandwidth

Above and in the text we consider phase-matched processes. If the AOM is driven at a different frequency Ω such that

$$\Delta \equiv K + \beta_1(\omega) - \beta_0(\omega + \Omega) \quad (53)$$

$$= 0, \quad (54)$$

the equations of motion become

$$\left(\mathbf{v}^{-1} \partial_t + \partial_z\right) \mathbf{a} = i g b e^{-\gamma z/2} \sigma_x e^{-i\Delta z} \sigma_z \mathbf{a}. \quad (55)$$

If $\Delta L \gg 1$, the light scattered between modes by the mechanics will destructively interfere and limit the total converted power.

We repeat the measurements and analysis presented in Fig. 4(c), varying the RF drive frequency and the optical wavelength away from a phase-matched operating point. The results are plotted in Fig. 1. While the RF bandwidth is dictated by the transducer response, the optical bandwidth (Fig. 1(b)) is determined by phase-matching. We simulate a data set from Eq. (55) using the measured values for $gt_{\text{b}\mu}L_{\text{eff}}$ and an optical group index difference $\Delta n_g = 0.175$. Fits to the simulated data are overlaid (red curve) on the measurements. The best-fit Δn_g is close to the FEM numerical value of 0.125.

3. Characterizing the AO Multiplexer

The performance of the multiplexers are summarized in the manuscript. Here we provide details on their characterization.

3.1. Transmission spectra of the optical couplers

The optical couplers are designed to adiabatically transfer the mode of the coupling waveguide into the AO waveguide. Widths of the two waveguides are chosen by solving for the modes of the adjacent waveguides as discussed in Section 3 of the manuscript. The tapered couplers are simulated by FDTD in Lumerical [10] and their insertion loss plotted in Fig. 2(a).

We measure the optical transmission through the device for the four optical paths $\text{TE}_{0/1} \rightarrow \text{TE}_{0/1}$, plotted in Fig. 2(b). Transmission through the TE_0 and TE_1 paths is similar. The peak efficiency of the grating couplers are independently measured to be -10 dB. The insertion loss of the device excluding the grating couplers is approximately -5 dB. The device exhibits -10 dB crosstalk into

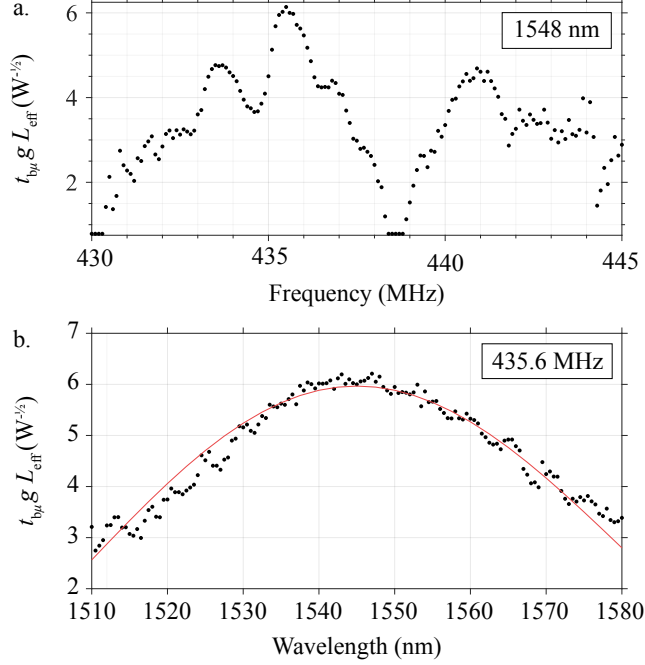


Fig. 1. **Optical and RF bandwidth of the AOM.** The measurements and regression presented in Fig. 4 are repeated over a range of wavelengths and RF frequencies to determine the bandwidth of the AOM. **a.** The RF response is largely determined by how the transducer, specifically $t_{b\mu}$, varies with Ω and so takes a shape similar to the transducer's conductance. **b.** Dispersion in the waveguide limits the optical bandwidth via the phase-matching condition. Measurements are in black. A dataset is simulated with the measured values for g , $t_{b\mu}$, and γ , and $\Delta n_g = 0.175$. It is fit to produce the red curve.

the unintended optical port. This crosstalk causes the optical pump to leak through into the signal channel. For example, if light is injected into the TE_1 port (bottom-left in Fig. 3), in a perfect device with no crosstalk only photons which absorb a phonon and scatter into the TE_0 mode leave from the bottom-right. With -10 dB crosstalk, 10% of the pump remaining at the end of the waveguide is sent into the bottom-right port. How the crosstalk is related to the scattering matrix of the optical couplers is explored in the next section.

The insertion losses for the different paths through the device are unequal which can arise from, *e.g.*, different efficiencies of the TE_0 and TE_1 optical couplers or variability in the fab. For example, $TE_1 \rightarrow TE_1$ can have a higher insertion loss than $TE_1 \rightarrow TE_0$. As a result, if light is fully converted from TE_1 to TE_0 by the mechanics, more light can leave the device with the drive on than with the drive off. The *modulation efficiency* as defined in Fig. 4(d) and Fig. 5(b) can exceed or not reach 0 dB at the full conversion drive power $P_{\pi/2}$.

3.2. Acousto-optic measurements of the optical couplers

The transmission spectra discussed in the previous section capture the total optical behavior of the device, but are insufficient to independently determine the crosstalk of the TE_0 and TE_1 couplers. We can use the acousto-optic signals to provide us with additional information. We ultimately find that the crosstalk of the TE_1 coupler dominates the crosstalk in Fig. 2.

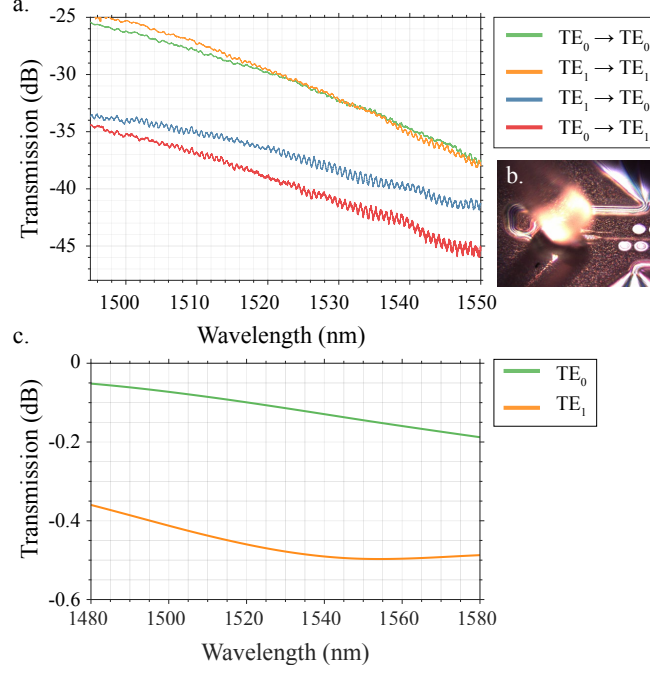


Fig. 2. **Optical transmission spectra of the modulator.** **a.** FDTD simulations of the insertion loss of both couplers. **b.** The transmission is measured aligning the fibers to each pair of optical ports. We observe -10 dB crosstalk. The center of the grating response is near 1500 nm. **c.** Photograph of a fiber coupled to the device.

Consider how light is transmitted through the device from left-to-right when the left transducer is driven. We construct a simple model for the optical transmission

$$a^{(\text{out})} = T^T \begin{pmatrix} \cos \zeta & -i \sin \zeta e^{-i\Omega t} \\ -i \sin \zeta e^{i\Omega t} & \cos \zeta \end{pmatrix} T a^{(\text{in})} \quad (56)$$

where

$$T = \begin{pmatrix} t_{00} & t_{01} \\ t_{10} & t_{11} \end{pmatrix} \quad (57)$$

describes optical transmission through the multiplexer and $a_i^{(\text{in})}$ is the complex amplitude of the light into port i where $i = 0$ for TE_0 and 1 for TE_1 . T includes the efficiency of the grating couplers. The off-diagonal components t_{10} and t_{01} are the amplitude transmission coefficients for the crosstalk of the TE_0 and TE_1 couplers, respectively. Unlike in the manuscript where the modes considered are at different frequencies, here we have explicit factors of $\exp(\pm i\Omega t)$ to keep track of emission/absorption of a phonon. For simplicity, we assume the two multiplexers are equivalent such that the one on the right is described by T^T .

If light is incident on the TE_0 port, $a^T = (1, 0)$, then

$$a^{(\text{out})} = \begin{bmatrix} (t_{00}^2 + t_{10}^2) \cos \zeta & -it_{00}t_{10}e^{-i\Omega t} \sin \zeta & -it_{10}t_{00}e^{i\Omega t} \sin \zeta \\ (t_{01}t_{00} + t_{11}t_{10}) \cos \zeta & -it_{01}t_{10}e^{-i\Omega t} \sin \zeta & -it_{11}t_{00}e^{i\Omega t} \sin \zeta \end{bmatrix}. \quad (58)$$

If light is incident on the TE₁ port, $a^\top = (0, 1)$, then

$$a^{(\text{out})} = \begin{bmatrix} (t_{10}t_{11} + t_{00}t_{01}) \cos \zeta & -it_{00}t_{11}e^{-i\Omega t} \sin \zeta & -it_{10}t_{01}e^{i\Omega t} \sin \zeta \\ (t_{11}^2 + t_{01}^2) \cos \zeta & -it_{01}t_{11}e^{-i\Omega t} \sin \zeta & -it_{11}t_{01}e^{i\Omega t} \sin \zeta \end{bmatrix}. \quad (59)$$

In each component, the first term proportional to $\cos \zeta$ describes the linear optics. The second is the upper sideband and the third is the lower sideband.

There are a couple things worth noting about these expressions. First, the crosstalk in the optical spectra in Fig. 2(a) is proportional to the crosstalk of the couplers. It is large if just one of the couplers has large crosstalk, *i.e.*, either t_{01} or t_{10} is large. In contrast, the sideband suppression is proportional to the product of the crosstalk of the couplers, $t_{01}t_{10}$. If just one of the couplers has low crosstalk, the spurious sideband will be suppressed. With regard to the optical couplers, low linear optical crosstalk is more demanding than sideband suppression.

We can measure each tone independently by heterodyne with the signal chain diagrammed in Fig. 4(a). The square of the above expressions for the transmitted amplitude is proportional to the power of the corresponding heterodyne signal. The following measurements were taken at $\Omega = 2\pi \times 441$ MHz and 1570 nm. Given our measurements of g , we remove the factors of $\cos \zeta$ and $\sin \zeta$ from Eqs. (58) and (59), leaving only the inferred optical insertion loss. The signals are renormalized by setting $P_{00}(0)$ to the measured optical insertion loss for the TE₀→TE₀ path. These values along with the scattering amplitudes are presented in Table 1.

Path	ω	$\omega + \Omega$	$\omega - \Omega$
TE ₀ →TE ₀	$t_{00}^2 + t_{10}^2$	$t_{00}t_{10}$	$t_{10}t_{00}$
	-27.0	-46.6	-46.8
TE ₀ →TE ₁	$t_{01}t_{00} + t_{11}t_{01}$	$t_{01}t_{10}$	$t_{11}t_{00}$
	-41.0	-47.1	-28.9
TE ₁ →TE ₀	$t_{10}t_{11} + t_{00}t_{01}$	$t_{00}t_{11}$	$t_{10}t_{01}$
	-39.6	-24.8	-45.7
TE ₁ →TE ₁	$t_{11}^2 + t_{01}^2$	$t_{01}t_{11}$	$t_{11}t_{01}$
	-26.3	-36.2	-38.2

Table 1. **Optical insertion loss measured by heterodyne.** We can use the heterodyne measurements to backout the scattering parameters of the optical multiplexers. Entries in the table are the amplitude transmission coefficient and the inferred optical insertion loss for the associated path in dB, both described in the text. From the table we can see that the left and right multiplexer have similar performance, and that the crosstalk measured in Fig. 2 is dominated by the crosstalk of the TE₁ coupler, t_{01} .

From the first and last rows in Table 1 we can see that the crosstalk of the TE₁ port, $|t_{01}|^2/|t_{11}|^2 = -10.9$ dB, is an order of magnitude worse than that of the TE₀ port, $|t_{10}|^2/|t_{00}|^2 = -19.7$ dB. From this model, we expect the sideband suppression to be -30.6 dB. Instead we observe -19.6 dB in the table but over -50 dB in Fig. 4(b) and roughly -40 dB in Fig. 5 of the main text.

In addition to optical crosstalk, mechanical reflections reduce the sideband suppression. If we sweep Ω as shown in Fig. 3, we find that the suppressed sideband exhibits high contrast fringes with a period on the order of a few MHz. This small period corresponds to mechanical delays

suggesting reflected phonons dominate over the optical crosstalk as a source of the spurious sideband.

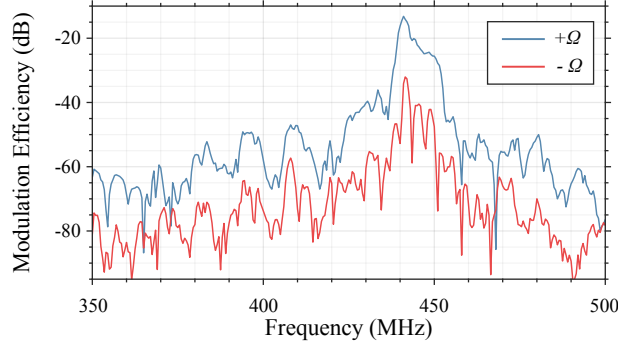


Fig. 3. **Fringes in the unmatched sideband** with varying mechanical frequency suggest that reflections of the mechanical wave play a leading role in determining the sideband suppression. These reflections dominate over the contribution arising from the AO multiplexer’s optical crosstalk. In this measurement, light is incident on the TE₁ port on the left and leaves the TE₀ port on the right. The left transducer is driven.

3.3. Piezoelectric transducer efficiency and mechanical propagation loss

The design of the transducer and methods for characterizing its efficiency and the mechanical propagation loss are described in detail in Refs. [9, 11]. The S-matrix of the device in Fig. 3 is measured on a calibrated probe station. From the reflection measurements S_{ii} where $i = 1$ for the left transducer and $i = 2$ for the right, we see that the response of the transducer is repeatable. The reflections (Fig. 4(a)) reach -2 dB for the SH₀ response corresponding to a -4.3 dB loss from impedance mismatch between the 50 Ω transmission line and transducer.

The single-port response is not enough to determine the transducer’s efficiency. There are other loss mechanisms in addition to impedance mismatch which reduce the transducer’s efficiency. Of the power emitted into the waveguide, nearly all of it is in the SH₀ mode but, as discussed in detail in Ref. [9], resonances in the transducer lead to large material damping losses. In order to determine the transmission coefficient $t_{b\mu}$ from microwaves in the line to phonons in the waveguide, we need to measure the two-port response S_{21} and filter out contributions from triple-transit, *etc.* [11]. In Fig. 4(c), we plot the raw S_{21} as well as the single-transit response filtered in the time-domain. This filtered signal is equal to $t_{b\mu}^2 e^{-\gamma L/2}$, assuming symmetric coefficients for the two transducers. The mechanical losses are independently determined by measuring how the transmission varies with the length of the waveguide L . These devices comprise a transducer-waveguide-transducer two-port network without the AO multiplexers. The impulse response h_{21} , *i.e.* the Fourier transform of S_{21} , is plotted in Fig. 5 where the peaks are fit (inset) for the propagation loss γ .

4. RF power-handling

The maximum conversion efficiency observed $\eta_{\max} = 18\%$ is limited by the microwave power-handling of the transducer and the AO multiplexer. In Fig. 6, we plot reflections from the transducer S_{11} measured on a vector network analyzer as the power is increased to 10 dBm at which η_{\max} was observed. As the power is increased, the center frequency of the IDT decreases and, for fixed-frequency drives, can cause drops above 1 dB. After removing the 1.2 dB round-trip loss in the cable, this change in S_{11} amounts to a -3 dB decrease in the power delivered to the

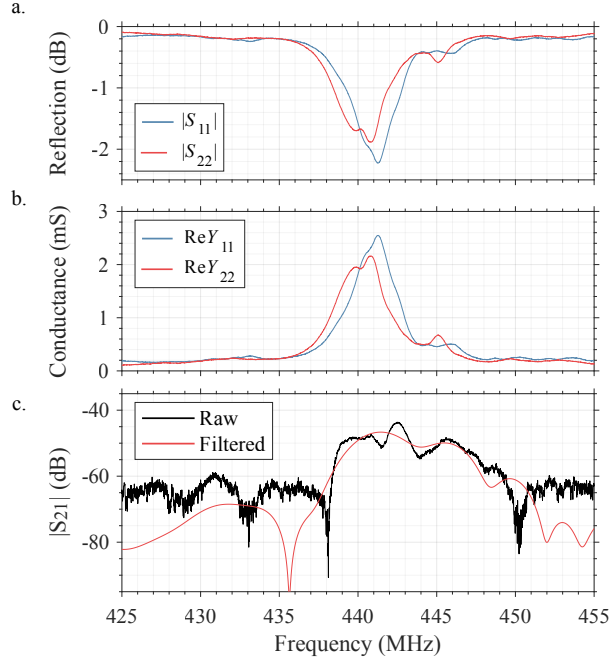


Fig. 4. **Transducer response and mechanical transmission.** The left and right transducer in Fig. 3 are ports 1 and 2, respectively. **a.** The dip in the reflections near 440 MHz corresponds to the SH_0 mode plotted in the bands in Fig. 1 of the manuscript. **b.** The conductance reaches 2 mS. **c.** We overlay the transmission S_{21} filtering out microwave crosstalk and higher-order transits in the device onto the raw data. The filtered response removes ripples from the higher-order transits and is used to extract $t_{b\mu}^2 e^{-\gamma L/2}$.

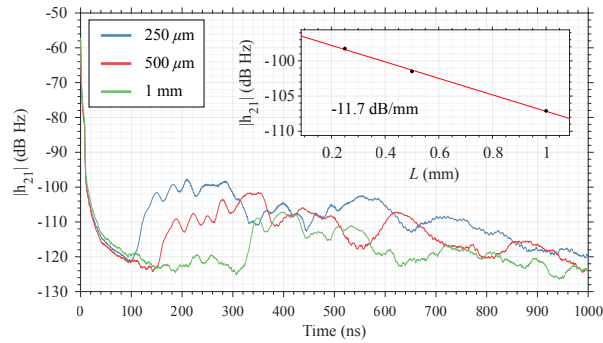


Fig. 5. **Mechanical propagation loss.** We extract the propagation loss from a length sweep of the waveguide by fitting a line to the magnitude of the impulse response. We fit an exponential to the peak response yielding $\gamma = 11.7$ dB/mm (inset).

device. This power-dependent frequency shift causes the curves in Fig. 4(c) to deviate from a sinusoid, and so we restrict our fits for $gt_{b\mu}$ to the low-power portion of the dataset. Not only do we see frequency shifts, at 10 dBm discontinuities appear in $S_{11}(\Omega)$, evidence of bi-stability arising from, *e.g.*, Duffing nonlinearities.

At 13 dBm drive power, the tethers in the multiplexer broke. The AO and coupling waveguides separated from one another, destroying the optical couplers.

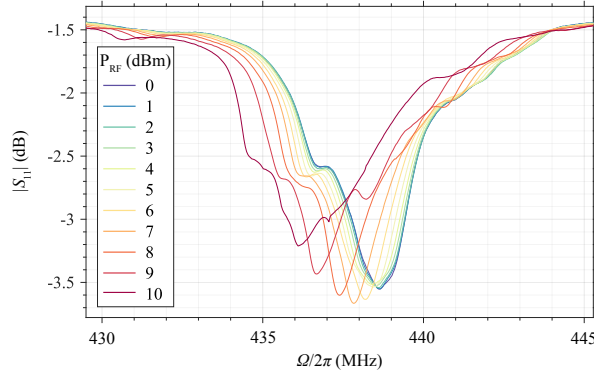


Fig. 6. **Power-handling of the transducer.** Microwave reflections S_{11} from the transducer show a center frequency shift and bi-stabilities as the drive power P_{RF} is increased to 10 dBm.

5. Inferring g

In our heterodyne measurements described in Section 5 of the manuscript, both the pump depletion and converted signal powers are measured, and both can be used to infer g . In the low-power limit, the pump depletion provides a better measure of the $P_{\pi/2}$. Given a pump with initial amplitude a_0 , the flux in the pump varies up to $O(\beta^5)$ as

$$|a_0|^2 \cos^2(gt_{b\mu}\beta L) \approx |a_0|^2 \left(1 - |gt_{b\mu}\beta L|^2 + \frac{1}{3} |gt_{b\mu}\beta L|^4 \right). \quad (60)$$

while the signal power varies as

$$|a_0|^2 \sin^2(gt_{b\mu}\beta L) \approx |a_0|^2 \left(|gt_{b\mu}\beta L|^2 + \frac{1}{3} |gt_{b\mu}\beta L|^4 \right). \quad (61)$$

Two terms in the series are needed to fit $g|t_{b\mu}|L$ without independently measuring $|a_0|^2$. This is satisfied for the pump to second-order in β but to fourth order for the signal, making pump depletion a more sensitive measure of the efficiency in the low-power limit.

The drives used for the dataset in Fig. 4 were high enough for independent regressions on the pump and converted signal to give comparable values for $P_{\pi/2}$.

References

1. A. Yariv, "Coupled-mode theory for guided-wave optics," IEEE J. Quantum Electron. **9**, 919–933 (1973).
2. J. Sipe and M. Steel, "A Hamiltonian treatment of stimulated brillouin scattering in nanoscale integrated waveguides," New J. Phys. **18**, 045004 (2016).
3. C. Wolff, M. J. Steel, B. J. Eggleton, and C. G. Poulton, "Stimulated Brillouin scattering in integrated photonic waveguides: Forces, scattering mechanisms, and coupled-mode analysis," Phys. Rev. A **92**, 013836 (2015).
4. S. G. Johnson, M. Ibanescu, M. Skorobogatiy, O. Weisberg, J. Joannopoulos, and Y. Fink, "Perturbation theory for Maxwell's equations with shifting material boundaries," Phys. review E **65**, 066611 (2002).

5. A. Andrushchak, B. Mytsyk, H. Laba, O. Yurkevych, I. Solskii, A. Kityk, and B. Sahraoui, "Complete sets of elastic constants and photoelastic coefficients of pure and MgO-doped lithium niobate crystals at room temperature," *J. Appl. Phys.* **106**, 073510 (2009).
6. A. W. Snyder and J. Love, *Optical waveguide theory* (Springer Science & Business Media, 2012).
7. B. A. Auld, *Acoustic fields and waves in solids*, vol. II (John Wiley & Sons, 1973).
8. I. Hinkov, V. Hinkov, and E. Wagner, "Low power integrated acousto-optical tunable filters in first telecommunication window," *Electron. Lett.* **30**, 1884–1885 (1994).
9. Y. D. Dahmani, C. J. Sarabalis, W. Jiang, F. M. Mayor, and A. H. Safavi-Naeini, "Piezoelectric transduction of a wavelength-scale mechanical waveguide," *Phys. Rev. Appl.* **13**, 024069 (2020).
10. Lumerical Inc., "**FDTD**: 3D Electromagnetic Simulator," (2019).
11. C. J. Sarabalis, Y. D. Dahmani, A. Y. Cleland, and A. H. Safavi-Naeini, "S-band delay lines in suspended lithium niobate," *J. Appl. Phys.* **127**, 054501 (2020).